RESEARCH ARTICLE

ADVANCED ENERGY MATERIALS
www.advenergymat.de

Strategically Modified Ligand Incorporating Mixed Phosphonate and Carboxylate Groups to Enhance Performance in All-Iron Redox Flow Batteries

*Gabriel S. Nambafu, Aaron M. Hollas, Peter S. Rice, Jon Mark Weller, Daria Boglaienko, David M. Reed, Vincent L. Sprenkle, and Guosheng Li**

Iron redox flow batteries (Fe-RFBs) hold significant promise for achieving cost-effectiveness and utilizing abundant materials for stationary energy storage applications. Here, a design of a novel Fe complex utilizing a nitrogenous phosphonate/carboxylate mixed ligand, N,N-Bis(phosphono methyl)glycine (BMPG), is presented to achieve high performance Fe anolyte. Compared to its all-phosphonate form, nitrilotri(methylphosphonic acid) (NTMPA), the new complex Fe(BPMG)$_2$ demonstrates a negatively shifted redox potential, resulting in ≈0.07 V (≈10%) increase in battery output voltage. Full battery testing paired with ferrocyanide catholyte demonstrates stable cycling (capacity degradation <0.0001%/cycle) over 730 consecutive charge/discharge cycles with Coulombic Efficiency of 100% at a current density of 20 mA cm^{-2} under near neutral pH (≈8). Of particular interest, density functional theory (DFT) studies and *operando* Raman measurements provide strong evidence supporting a molecular structure in BPMG, which reveals the mixed phosphonate/carboxylate groups in BPMG maintain the octahedral coordination of the Fe ion center with phosphonates exclusively, while leaving the carboxylate unbound for both Fe(II) and Fe(III) complexes. This structural similarity between BPMG-based Fe(II) and Fe(III) complexes effectively mitigates the slow redox reaction kinetics observed in Fe(NTMPA)$_2$ anolyte, where significant ligand reorientation occurs between Fe(II) and Fe(III) complexes.

1. Introduction

Redox flow battery (RFB), an electrochemical energy storage technology utilizing solvated redox-active materials in its electrolytes, have shown great potential as stationary energy storage solutions in integrating intermittent renewable power sources, enhancing grid reliability, and reducing greenhouse gas emissions in the power sector.[1] Among its many features, including flexibility, scalability, and the decoupling of power and energy density, the most unique feature of flowable electrolytes undoubtedly lies at the core, from which the flow battery name was originated.[1,2] Undoubtedly, compared to other conventional static-state batteries, solvation or coordination chemistry in electrolytes has played critical roles in developing synthesis methods and understanding the fundamental redox reaction dynamics/kinetics governing in RFBs.[3] Among many proposed RFB systems, the all-vanadium RFB system (VRFB) stands out for its excellent electrochemical activity, reversibility, and scalability.[4] For example, recent advancements in VRFB research, such as the utilization of mixed acids (sulfuric acid/hydrochloric acid) as electrolytes, have resulted to significant improvements in performance and durability compared to conventional VRFB systems using sulfuric acid alone. In brief, the addition of hydrochloric acid introduces chloride anions that promotes the formation of $VO_2Cl(H_2O)_2$ neutral complex instead of $[VO_2(H_2O)_3]^+$ complex in the catholyte. The proposed coordination structure of $VO_2Cl(H_2O)_2$ neutral complex is believed to be less susceptible to deprotonation and condensation reactions, thus mitigating VRFB degradation—the formation of $V_2O_5{\cdot}3H_2O$ precipitate that is detrimental to the VRFB.[5]

Exploring RFB systems to incorporate more low-cost materials, such as iron (Fe), has the tremendous potential to alleviate supply chain constraint given its abundant resources and scaled mining/processing capabilities.[6] One important aspect to consider when comparing all soluble Fe-RFB to VRFB is that the valence states of Fe used in all soluble Fe-RFBs (**Figure 1**a), excluding conventional Fe flow batteries using Fe plate as the anode,[7] are typically limited to Fe(II) and Fe(III), which arise from Fe metal and the less stable higher oxidation states of Fe (e.g., ferrates) in aqueous solution. It's worth mentioning that the redox potential of Fe(II)/Fe(III) complexes can be altered, and its value is closely related to the equilibrium/formation

G. S. Nambafu, A. M. Hollas, J. M. Weller, D. Boglaienko, D. M. Reed, V. L. Sprenkle, G. Li
Energy and Environment Directorate
Pacific Northwest National Laboratory
Richland, WA 99354, USA
E-mail: guosheng.li@pnnl.gov

P. S. Rice
Physical and Computational Science Directorate
Pacific Northwest National Laboratory
Richland, WA 99354, USA

The ORCID identification number(s) for the author(s) of this article can be found under https://doi.org/10.1002/aenm.202403149

DOI: 10.1002/aenm.202403149

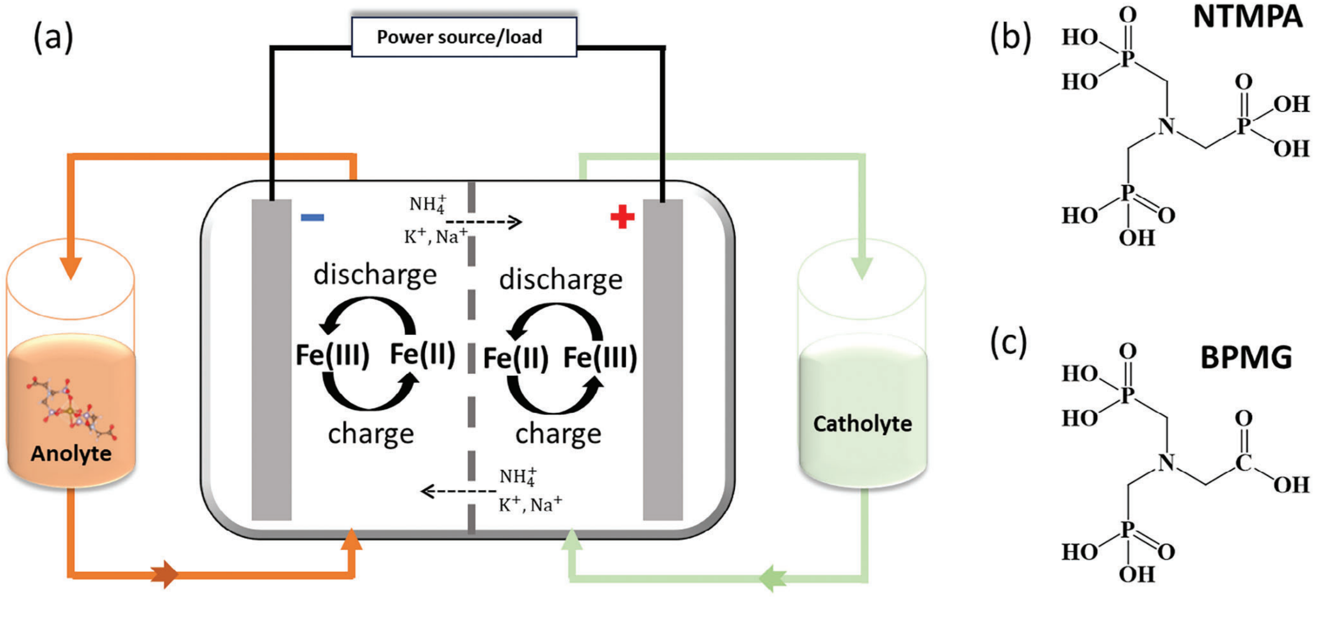

$$\text{Negative electrode: } Fe(II)(BPMG)_2 - e^- \leftrightarrow Fe(III)(BPMG)_2$$
$$\text{Positive electrode : } Fe(CN)_6^{3-} + e^- \leftrightarrow Fe(CN)_6^{4-}$$

Figure 1. a) Schematic of all-soluble iron based redox flow battery displaying the redox reactions, counter ions involved and chemical structure of b) BPMG ligand, c) NTMPA ligand.

constants of Fe(II) and Fe(III) complexes.[8] Therefore, strategically designing different Fe(II)/Fe(III) complex redox pairs with large redox potential biases for the catholyte and anolyte, respectively, is critical to achieve high voltage output in all soluble Fe-RFBs. Figure 1a displays a schematic representation of all soluble Fe-RFB highlighting key features such as the corresponding redox reaction on both electrodes and cation transfer during the charge and discharge process. Various ligands, such as triethanolamine (TEA),[9] cyclopentadienyl ($-C_5H_5$),[10] cyanide (−CN),[11] bipyridine(bpy),[12] among others,[8b,13] and their derivatives have been studied and proposed to prepare Fe complexes for Fe-RFB applications. For instance, $[Fe(TEA)OH]^-$/ $[Fe(TEA)OH]^{2-}$ (Fe-TEA, −0.86 V vs standard hydrogen electrode (SHE)) has been reported in the literature for use as anolyte, while pairing with $Fe(CN)_6$ (0.36 V vs SHE) as catholyte.[9b] However, several parasitic reactions, including Fe plating at the anode, TEA cross over, and contamination on membrane, have been reported for Fe-TEA complexes that severely limit the long-term cyclability as all-soluble Fe-RFB applications. Another example is using Na[Fe-N,N'-ethylene-bis-(o-hydroxyphenylglycine)] (Na[Fe-racEDDHA]), which has a reversible redox potential at −0.61 V versus Ag/AgCl, making it suitable for use as an anolyte. However, preparing Na[Fe-racEDDHA] requires an extensive purification step involving column chromatography to separate it from the stereoisomers. Moreover, the low solubility of this complex and uncertainty in its longevity require further electrolyte optimization and rigorous long-term cycling test for the practical applications.[14] As well, asymmetric bi-ligand iron complex was investigated as catholyte in a Zn-Fe flow battery. The synergy between pyridine and disodium 4,5-dihydroxy-1,3-benzenedisulfonate ligands facilitated improved stability and performance by mitigating complex precipitation and improving mass transfer of the redox species.[15]

More recently, a nitrogenous triphosphonate ligand has been proposed and tested for the first time in the preparation of the anolyte for near-neutral pH all-soluble Fe-RFBs. The resulting complex, iron nitrilotri(methylphosphonic acid) ($Fe(NTMPA)_2$), prepared from low-cost and abundant materials, has demonstrated a solubility (0.67 M) and long-term cycling stability (1.3% over 1000 cycles), making it an appealing choice for all-soluble Fe-RFB application.[16] It is worth mentioning that the average output voltage of all-soluble Fe-RFB consisting of $Fe(NTMPA)_2$ anolyte and ferrocyanide ($Fe(CN)_6$) catholyte is ≈0.6 V, which is slightly lower than that from reported Fe based flow batteries,[9,14,17] and conventional VRFBs.

Additionally, density functional theory (DFT) studies of $Fe(NTMPA)_2$ have proposed that the distinctive voltage plateau observed exclusively during the charging process of the $Fe(NTMPA)_2$ anolyte under higher current densities could be ascribed to the peculiar ligand reorientation between $Fe(III)(NTMPA)_2$ and $Fe(II)(NTMPA)_2$ complexes, arising from the different preferences in molecular structures. This preference for molecular structure stems from the fact that NTMPA (Figure 1b) possesses three phosphonate ($-PO(OH)_2$) functional groups, which promote structural reorganization via a transition from two to all three phosphonate groups being involved in coordination to form the Fe complexes during the redox reaction.[16] To further enhance the performance of NTMPA-based Fe-RFBs, strategic design of new ligands is necessary to mitigate kinetic issues from ligand reorientation.

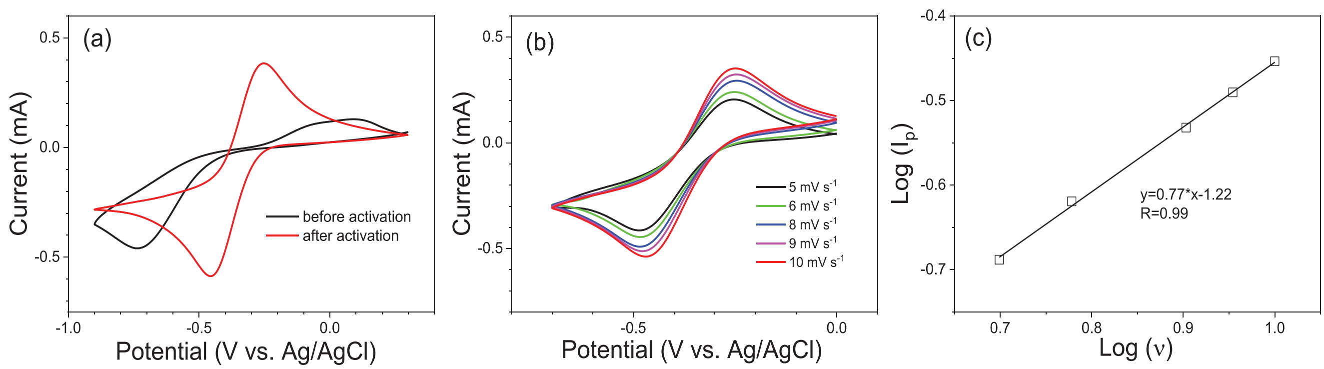

Figure 2. Cyclic voltammetry measurements and analysis. a) CV plots of 0.3 м $Fe(BPMG)_2$ complex using standard and activated glassy carbon electrode b) CV of $Fe(BPMG)_2$ complex at different scan rates, and c) plot of log anodic peak current (I) versus log scan rate (v).

Here, we replace a phosphonate of NTMPA with a different moiety, such as carboxyl (–COOH)-based ligand, to form N,N-Bis(phosphonomethyl)glycine (BPMG, Figure 1c), striving to solve the unique voltage step up phenomenon and kinetic problem encountered in the $Fe(NTMPA)_2$ complex. The rationale behind this approach is that the third phosphonate in the ligand NTMPA may exhibit a stronger binding affinity compared to that of the carboxylate in BPMT, owing to the higher pKa value of phosphonate that is in a stronger conjugate base compared to carboxylate. Consequently, this potentially leads to the formation of a single complex structure with the free carboxylate positioned away from the octahedral Fe coordination shell, which is supposedly surrounded by two phosphonates. The new iron complex—$Fe(BPMG)_2$ at near-neutral pH (≈8), demonstrated a more negatively shifted redox potential by ≈0.07 V, which results in higher battery output voltage, compared to that of previously reported $Fe(NTMPA)_2$ anolyte. Full cell testing demonstrated over 700 consecutive charge and discharge cycles with Coulombic Efficiency (CE) of 100% at a current density of 20 mA cm^{-2}. More importantly, the battery kinetic testing results indicate that replacing NTMPA with BPMG ligand help to constrain the complex structure thus resolving the kinetics limitation observed for $Fe(NTMPA)_2$ anolyte. O*perando* Raman spectroscopy results substantiate DFT findings and provide deep understanding of these complexes and their structural differences/changes at different state of charge (SOC) without interrupting the battery cycling. This work provides a pathway for ligand modification to develop ideal complexes for high performance aqueous Fe-RFBs

2. Results and Discussion

First, the electrochemical measurements of $Fe(BPMG)_2$ were evaluated using cyclic voltammetry (CV) to determine its redox properties, and its suitability as an anolyte in Fe-RFBs. The pretreatment and activation of the glassy carbon (GC) electrode through surface oxidation proved crucial in the CV study of the $Fe(BPMG)_2$ electrolyte. A shown in **Figure 2a**, CV results employing activated GC electrode displays excellent reversibility in comparison to untreated GC electrode.[18] CV plot of $Fe(BPMG)_2$ at a scan rate of 10 mV s^{-1} reveals a typically well-defined redox peaks with an anodic peak at −0.25 V and a cathodic peak at −0.45 V, respectively. CVs were also conducted at various scan rates, i.e., 5, 6, 8, 9, and 10 mV s^{-1}, and display a trend of increasing current with higher scan rate in Figure 2b. A brief analysis (Figure 2c) via linear fitting for the plot of log of peak current (*I*) versus log scan rate (n) shows a slope of 0.77, suggesting that the kinetics of $Fe(BPMG)_2$ redox reaction is both diffusion and a mass transfer controlled.[19] A comparison of CV between $Fe(BPMG)_2$ and $Fe(NTMPA)_2$ (Figure S1a, Supporting Information), a previously reported complex, was also carried out under similar conditions, i.e., 0.3 м electrolyte concentration and using activated GC electrode. $Fe(BPMG)_2$ and $Fe(NTMPA)_2$ complexes exhibited half potentials of ≈−0.36 and −0.29 V respectively, indicating a possible higher voltage output for $Fe(BPMG)_2$ compared to $Fe(NTMPA)_2$ electrolyte. Additionally, scan rate dependence studies of $Fe(BPMG)_2$ and $Fe(NTMPA)_2$ as shown in Figure 2b and Figure S1a (Supporting Information) were conducted. A plot of the peak currents reveals a linear relationship with the square root of the scan rates for both $Fe(BPMG)_2$ and $Fe(NTMPA)_2$ complexes as shown in Figure S1b,c (Supporting Information) respectively. The diffusion coefficients were derived according to Randles-Sevcik equation (Equation S1, Supporting Information) and yields values of 7.53×10^{-7} and 2.58×10^{-8} cm^2 s^{-1} for $Fe(BPMG)_2$ and $Fe(NTMPA)_2$ complexes respectively. This will be further elaborated with the studies from EIS and DFT calculations in the following section.

A full cell testing was carried by pairing $Fe(BPMG)_2$ anolyte with $Fe(CN)_6$ as catholyte to evaluate the charge/discharge performances and the long-term stability of this battery chemistry. As mentioned in the experimental section, the test was done at a constant current (CC) of 200 mA (20 mA cm^{-2}), thenceforth, constant voltage (CV) of 1.0 and 0.3 V for the charge and discharge processes until the current reaches 10 mA. As shown in **Figure 3a**, the battery testing demonstrates more than 700 successive charge and discharge cycles (≈25 days) with a Coulombic Efficiency (CE) of 100%, and no apparent capacity fade (<0.0001%/cycle) is observed under CC+CV cycling mode. A cell with larger volume electrolytes (50 ml, Figure S2, Supporting Information) was also tested at current density of 20 mA cm^{-2} for up to 100 cycles, showing a stable capacity trend and high CE similar to that observed in small volume cell testing. Cell voltage profiles of each charge and discharge process at 1st, 250th, 500th, and 730th cycles are compared in Figure 3b. An observation from these voltage profiles is that the overpotential during the charge/discharge process increases over the long-term cycling. One potential explanation for the observed

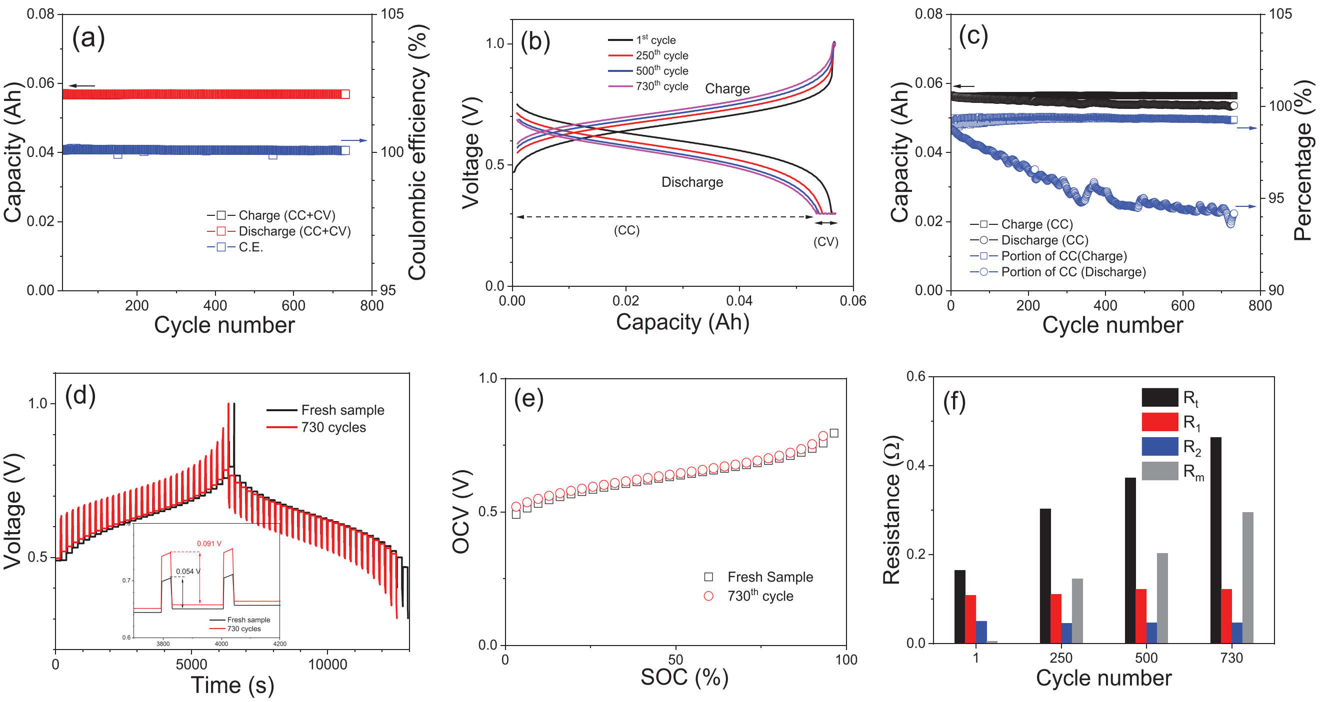

Figure 3. Cycling data and pulse-rest cycle measurement for the cell consisting of 0.3 м $Fe(BPMG)_2$ anolyte and 0.3 м $Fe(CN)_6$ catholyte. a) The total capacity (CC+CV) and Coulombic efficiency (CE) for the accelerated test over 730 cycles (≈25 days) with a current density at 20 mA cm^{-2}. See the main text for CC+CV cycling conditions. b) Voltage profiles of charge and discharge of 1^{st}, 250^{th}, 500^{th}, and 730^{th} cycle. CC and CV portion of the discharge are shown by the arrow lines as example, respectively. c) The capacity of CC portion and its percentage over the total capacity (CC+CV) are plotted for the charge and discharge over 730 cycles, respectively. d) pulse-rest plots for the fresh and cycled (730^{th} cycle) of $Fe(BPMG)_2/Fe(CN)_6$ cell, respectively. Typical zoom-in view of pulse-rest (current pulse + resting period) plots for the fresh and cycled cell as an insert. e) Open circuit voltage (OCV) profiles for the fresh and cycled cell. f) Comparison of R_1 (Ohmic resistance), R_2 (charge transfer resistance), R_m (mass transfer resistance), and R_t (overall resistance) for $Fe(BPMG)_2/Fe(CN)_6$ cell at 50% state of charge (SOC) over the long term cycling.

overpotential, particularly in this study, could be an escalation in cell resistance. This could potentially cause from diverse factors, such as a reduction in the active surface area of the electrode and flow rate due to clogging. This phenomenon is illustrated in Figure S3 (Supporting Information), providing clear evidence of deposition on the cell stack following the extended cycling test. It appears that the clogging was most likely caused by peeling off from the peristaltic tubes used in the flow battery setup, and it occurs more rapidly during the early stages of cycling. For instance, the growth of the overpotential is quicker between 1^{st} and 250^{th} cycle compared to the rest of cycles. Another observation from Figure 3b is that the duration of the CV portion of discharge is increasing over the cycling, whereas the CV portion of the charge shows minimal change. To quantitatively illustrate the trend of charge and discharge CE, Figure 3c present the capacity of charge and discharge, as well as the respective proportions relative to the full capacity (CC+CV). It's interesting to observe that there is negligible loss (<0.0001%/cycle) in CC charge capacity, while there is a decrease of ≈6% in CC discharge capacity after 730 cycles (0.008%/cycle). Table S1 compares the features and performances of $Fe(BPMG)_2$ based flow battery and other all-soluble all-iron flow battery. It is noteworthy that the decrease in capacity within the CC portion of the discharge is primarily attributed to kinetic constraints rather than permanent loss. This is evident as it is recuperated during the constant voltage (CV) period for each cycle, resulting in no total capacity loss (CC+CV), as shown in Figure 3a. Pulse-rest experiment was employed with a pulse charge/discharge period of 0.0016 Ah (≈33 s) and a rest time of 180 s. Figure 3d shows two pulse-rest curves during the charge and discharge processes for the battery with fresh $Fe(BPMG)_2$ anolyte and after 730 cycles, with a typical zoomed-in view of the curves between 3500 and 4200 s. The zoomed-in plot reveals a 0.054 V overpotential for the fresh electrolyte and a subsequent increase to 0.094 V for the cycled electrolyte at the 730^{th} cycle, agreeing well with the higher overpotential observed for larger cycle numbers as shown in Figure 3b. Subsequently, we picked out the voltage value at the last point of each resting period to bring forth the open circuit voltage (OCV) profile as shown in Figure 3e. The OCV profile with eliminating the overpotential, demonstrates a comparable cell voltage profile between the fresh and cycled electrolytes. This suggests no significant change in battery chemistry or electrolyte composition after long term cycling, consistent with the battery cycling results (Figure 3a). Figure 3f shows the comparison of R_t, R_1, R_2, and R_m over the long-term cycling. R_t is obtained by subtracting OCV (Figure 3e) from each charge voltage profile shown in Figure 3b, then dividing by the current (200 mA). R_1 (ohmic resistance) and R_2 (charge transfer resistance) were obtained by fitting the Nyquist plots of impedance spectra shown in Figure S4 (Supporting Information), which the fitted data listed in Table S2 (Supporting Information). R_m, a resistance due to over polarization related to mass transfer, is obtained by subtracting R_1 and

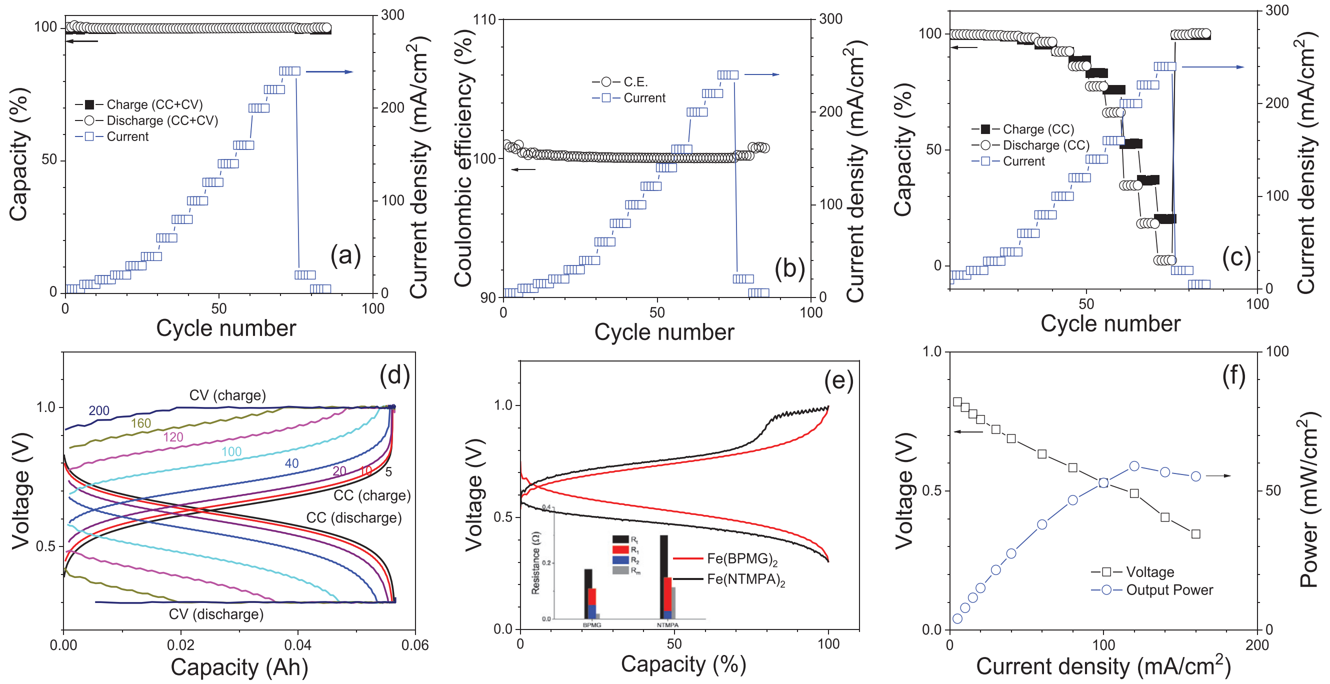

Figure 4. Battery testing at different current densities a) The total capacity plots of CC and CV at different current densities, b) CE, c) CC capacity for charge and discharge, d) charge/discharge voltage profiles, e) comparison of charge/discharge profiles at current density of 60 mA cm^{-2} for Fe(BPMG)$_2$ and Fe(NTMPA)$_2$. Comparison of resistances (R_t, R_1, R_2, R_m) for Fe(BPMG)$_2$ and Fe(NTMPA)$_2$ are shown as insert. and f) the battery discharge voltage and discharge power density at 100% SOC.

R_2 from R_t. It is interesting to note that R_1 and R_2 show minimal change over long-term cycling, indicating that the membrane and charge transfer properties remain unchanged. Majority of the increase of cell over polarization during cycling (Figure 3b) or the rise in R_t, overall resistance, can be attributed to the increased R_m, which can be influenced by various factors, including change of flow dynamic caused by clogging of cell stack described above.

The rate capability of the Fe(BPMG)$_2$ anolyte was assessed under CC+CV mode, revealing minimal degradation in total (CC+CV) charge and discharge capacity (**Figure 4a**) across various current densities (5–240 mA cm^{-2}). Also, CE (Figure 4b) remains consistently near 100% throughout testing. However, when plotting only the charge and discharge capacities (Figure 4c) of the CC portion, a clear decrease in capacity with increasing current density is evident, which is attributed to its intrinsic kinetic response. Notably, capacity is restored when current is reduced to lower values, such as 5 and 10 mA cm^{-2}, indicating the excellent stability of Fe(BPMG)$_2$ anolyte and absence of decomposition during the high current density cycling. The energy efficiency varies at different current density as shown in Figure S5b (Supporting Information). It's worth noting that the capacity retention of the CC step during charge appears slightly better than that of discharge, aligning well with the larger capacity degradation rate illustrated in Figure 3c, and this observation suggests that Fe(BPMG)$_2$ intrinsically exhibits slightly faster redox kinetics for the charge process. Figure 4d presents the charge and discharge voltage profiles at various current densities, illustrating a shortening in the voltage profiles of the CC portion compared to the elongation of the CV portion due to higher overpotentials for the charge and discharge with increasing current density. Furthermore, unlike Fe(NTMPA)$_2$ reported in the previous work, Fe(BPMG)$_2$ displayed a consistent single voltage plateau across various current densities.[16] This suggests the presence of a single charge pathway for Fe(BPMG)$_2$ participating in the redox reaction, contrasting with two charge pathways reported in the previous work for Fe(NTMPA)$_2$. A direct comparison (Figure 4e) of the voltage profiles of Fe(NTMPA)$_2$ and Fe(BPMG)$_2$ anolytes at the same testing condition (60 mA cm^{-2}) is provided to highlight the difference in charge voltage profiles, where a voltage step-up is clearly observed for Fe(NTMPA)$_2$ in contrast to a smooth voltage profile for Fe(BPMG)$_2$. Resistances obtained using the same method described in Figure 3f are compared for Fe(BPMG)$_2$ and Fe(NTMPA)$_2$ cells. The sum of R_1 and R_2 shows no drastic difference (or slightly smaller) for Fe(BPMG)$_2$ compared to that of Fe(NTMPA)$_2$ (Figure S6, Supporting Information for EIS data). In contrast, R_m of Fe(BPMG)$_2$ is much smaller than that of Fe(NTMPA)$_2$ cell, which aligns well with the larger diffusion coefficient of Fe(BPMG)$_2$ shown above. Further details about this variance in redox reaction mechanism will be discussed in the following section with the support of DFT and *operando* Raman Spectroscopy. Figure 4f illustrates that the discharge capability of the 0.3 M Fe(BPMG)$_2$ anolyte at 100% SOC exhibits an output power density of 53 mW cm^{-2} at a current density of 100 mA cm^{-2}, outperforming the comparable power density obtained from higher concentration Fe(NTMPA)$_2$ at 0.67 M,[16] supporting possible faster redox reaction kinetics of Fe(BPMG)$_2$.

To understand how the difference in molecular structures between BPMG and NTMPA could affect the redox chemistries in Fe-RFB, we have performed a series of DFT simulations. Specifically, we have explored several possible coordination environ-

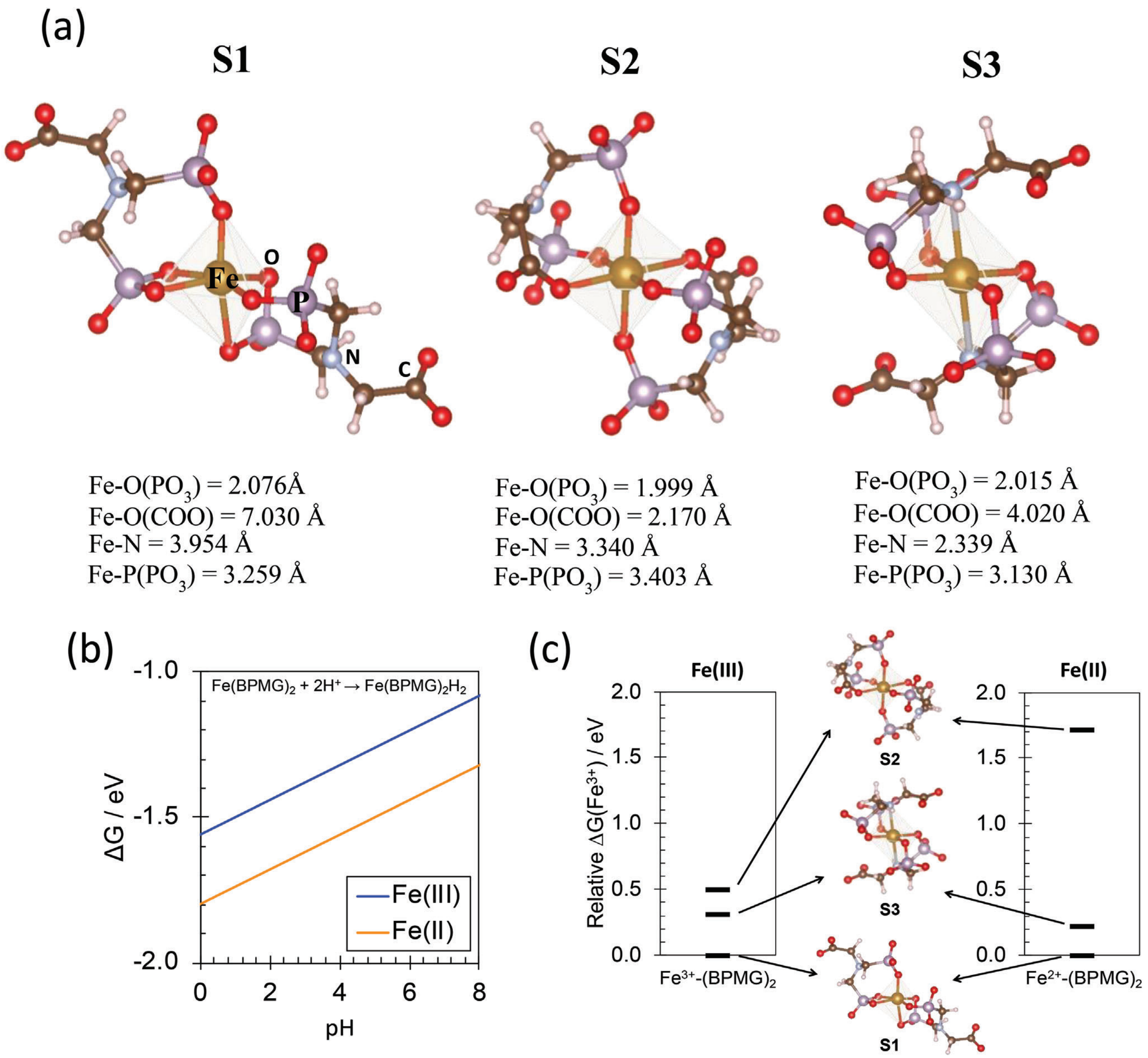

Figure 5. DFT studies for $Fe(BPMG)_2$ complexes. a) DFT optimized geometries for $Fe(BPMG)_2$ in the most feasible bonding configurations S1, S2, and S3. Structural information is provided for the ligands, which are bound to the central iron species in the distorted octahedral environment. b) Calculated free energy diagram for the protonation of nitrogen atoms in BPMG in the Fe(III) and Fe(II) oxidation states as a function of pH. c) Relative free energy (ΔG) diagrams for several possible coordination environments for $Fe(BPMG)_2$ to account for conformational changes which may occur during the charging and discharging process.

ments for $Fe(BPMG)_2$ to capture any conformational changes that may occur during the charge and discharge process, denoted as S1, S2, and S3 (**Figure** 5a). Our calculations predict that both the Fe(III) and Fe(II) complex is most stable in the high-spin sextet and septet states respectively, shown in Figure S7 (Supporting Information). This observation is consistent with the phenomenon of peak broadening observed in NMR spectra (Figure S8, Supporting Information), attributed to the paramagnetic features of high-spin Fe complexes.[20] The structures reported in Figure 5a display significant structural resemblances to $Fe(NTMPA)_2$ reported previously, while also presenting distinct variations ligand coordination denticity. For instance, $Fe(BPMG)_2$ in the S1 configuration, results in two phosphonate groups of each BPMG bonded in a bidentate-monodentate configuration with the central Fe, leaving a dangling unbound carboxylate group. This configuration resembles our previously reported structure for $Fe(NTMPA)_2$,[16] which has one unbounded phosphonate group instead of a carboxylate in $Fe(BPMG)_2$. Despite the similarities in the inner sphere coordination environment between BPMG and NTMPA in the S1 state, the dangling carboxylate group in BPMG will influence outer sphere coordination of counter ions when compared with the phosphonate group in NTMPA. $Fe(BPMG)_2$ in the S2 configuration, shown in Figure 5a, has all three functional groups (two phosphonates and one carboxylate) involved in the coordination with Fe, each acting as a monodentate ligand. From Figure 5b under the battery cycling condition near pH 8, the nitrogen atoms of BPMG undergo protonation, leading to their existence in a Zwitterionic state. This effectively inhibits the bonding capability of nitrogen atoms, which is essential for the molecular structure of S3, see Supporting Information for more details. Consequently, the most viable molecular structures for $Fe(BPMG)_2$ are likely to be found in S1 and S2. The relative free energy diagrams (Free energy calculation presented in Equation S2, Supporting Information) for the S1 and S2 structures of $Fe(II)(BPMG)_2$ and $Fe(III)(BPMG)_2$ are shown in Figure 5c, clearly illustrating the preference for the S1 molecular structure, which has a much lower free energy compared to S2 molecular structure. This preference is characterized by the presence of free carboxylate acting as non-bonding ligand with both Fe(II) and Fe(III) ion centers.

In order to experimentally observe the presence of non-bonding carboxylate in $Fe(BPMG)_2$ complex, *operando* Raman spectroscopy (**Figure 6**) was conducted in this work. The detailed experimental setup and spectra analysis method can be found in the experimental section. This technique enabled us to monitor the characteristic Raman bands from Fe complexes (Figure 6a), focusing particularly on the signals originating from carboxylate groups without interrupting the battery cycling process. In Figure 6b, a typical intensity map is shown, comprising 200 *operando* Raman spectra collected across a full charge (0–100% SOC) and discharge cycle (100–0% SOC). In other words, the lower half of the spectra represent the charge cycle, while the upper half represent the discharge cycle. It is noteworthy that certain Raman bands, especially those associated with P–O bonds, observed during *operando* measurements, demonstrate intensity variations correlating with changes in SOC. Remarkably, these variations appear to be highly reversible, which aligns well with the good cyclability observe in the $Fe(BMPG)_2$ flow battery (Figure 3a). Five *operando* Raman spectra at different SOCs, 0, 25, 50, 75, and 100% SOC are shown as representatives in Figure 6a. Instead of going into extensive detail about Raman band assignment, which exceeds the scope of this work, we briefly allocated Raman bands primarily associated with the P–O stretch mode of phosphonate and the vibration modes from carboxylate.[21] For example, the P–O stretch at 985 cm^{-1} linked with $Fe(II)(BPMG)_2$ demonstrates a trend of intensification with increasing SOC. Conversely, the P–O band associated with the $Fe(III)(BPMG)_2$ complex, located between 1000–1060 cm^{-1}, displays an inverse trend, with its intensity decreasing as SOC increases. Furthermore, the peak shift observed in the P–O stretch mode of $Fe(III)(BPMG)_2$ compared to $Fe(II)(BPMG)_2$, ranging from 15–75 cm^{-1}, aligns well with a similar peak shift ($\approx$22 cm^{-1}) previously reported for the $Fe(NTMPA)_2$ complexes using FT-IR spectra.[16] The intensities of the 985 and 1042 cm^{-1} bands were plotted against SOCs, revealing a good correlation that aligns well with linear fittings (see Figure 6a insert). This observation suggests the potential for on-line monitoring of SOCs using appropriately integrated Raman probes, with minimal technical challenges or complexities in practical applications. In contrast to the periodic change observed in the intensity and wavenumber of Raman bands associated with the P–O stretch of phosphonate, which are significantly influenced by the binding of either Fe(II) or Fe(III) depending on the SOCs of the battery, the Raman bands associated with carboxylate, such as 935 cm^{-1} ($-COO^-$ out of plane mode) and 1320/1399 cm^{-1} ($C-O^-$ stretch mode), remain unchanged in both intensity and peak position. This suggests that the carboxylate group of the BPMG ligand does not directly participate in complexation within the octahedral coordination with Fe ions. Instead, it most likely exists as a non-bonding moiety among three functional groups (two phosphonates and one carboxylate) of the BPMG ligands, which aligns well with S1 molecular structure suggested from DFT calculation. This preference for the S1 molecular structure in both $Fe(II)(BPMG)_2$ and $Fe(III)(BPMG)_2$, as opposed to $Fe(NTMPA)_2$ which exists in both S1 and S2 molecular structures for $Fe(III)(NTMPA)_2$ complex, plays a vital role in distinguishing the redox reaction performance mentioned above. Following a similar rationale, if we consider faster electron transfer kinetics for complexes that entail minimal structural changes or ligand reorientation in the first coordination shell, it becomes evident that the redox reaction of $Fe(BPMG)_2$ undergoes little to no ligand reorientation comparing to $Fe(NTMPA)_2$. This consequently results in fewer kinetic constraints or no additional high voltage plateau during the charge process under the high current densities for $Fe(BPMG)_2$ compared to that appearing for $Fe(NTMPA)_2$, as shown in Figure 4e. In addition, XANES spectra confirms the BPMG ligand doesn't take part in the redox reaction, only Fe metal center is involved. Figure S9 (Supporting Information)exhibits ex situ x-ray absorption spectroscopy (XAS) measurements, employing Fe K-edge XAS to ascertain the oxidation states of Fe through X-ray absorption near-edge structure (XANESedges. $Fe(BPMG)_2$ anolytes sampled at different SOCs, ranging from 0% to 100% SOC were analyzed to generate these measurements. As displayed, XANES peaks shift to the left (lower energy) while SOCs change from 0% SOC (Fe(III)), to 100% SOC (Fe(II)). The calculated SOCs (Table S3, Supporting Information) from the linear combination analysis are 27%, 52%, and 76%, respectively, and are in consensus with the SOCs determined through coulomb counting (cell testing).

Despite the higher voltage output and faster redox kinetics of $Fe(BPMG)_2$ anolytes compared to $Fe(NTMPA)_2$ anolytes reported earlier, it should be noted that $Fe(BPMG)_2$ anolyte still encounters some obvious challenges, such as solubility. For example, we observed that increasing the concentration of $Fe(BPMG)_2$ from 0.3 to 0.67 M likely leads to the precipitation of $Fe(II)(BPMG)_2$ at 100% SOC, as evidenced by visual inspection and the limited discharge capacity followed by a full charging process, as shown in Figure S10a (Supporting Information). While increasing the concentration of $Fe(BPMG)_2$ is not a trivial task, optimizing electrolyte conditions (pH, counter cations, ligand functionalization etc.) could be a viable route to alter the solubility that ultimately increases the energy density and reduces the cost of the RFB. As an illustration, use of K^+ as the counter ion enabled battery testing at high solubility of 0.67 M without precipitation as shown in Figure S10b (Supporting Information). Further performance optimization of this battery chemistry will be explored more in future. Considering the feasibility of large-scale production, both BPMG and NTMPA are commercially available at relatively low cost. NTMPA is derived from ammonia, formaldehyde, and phosphorous acid, whereas BPMG can be synthesized from cost

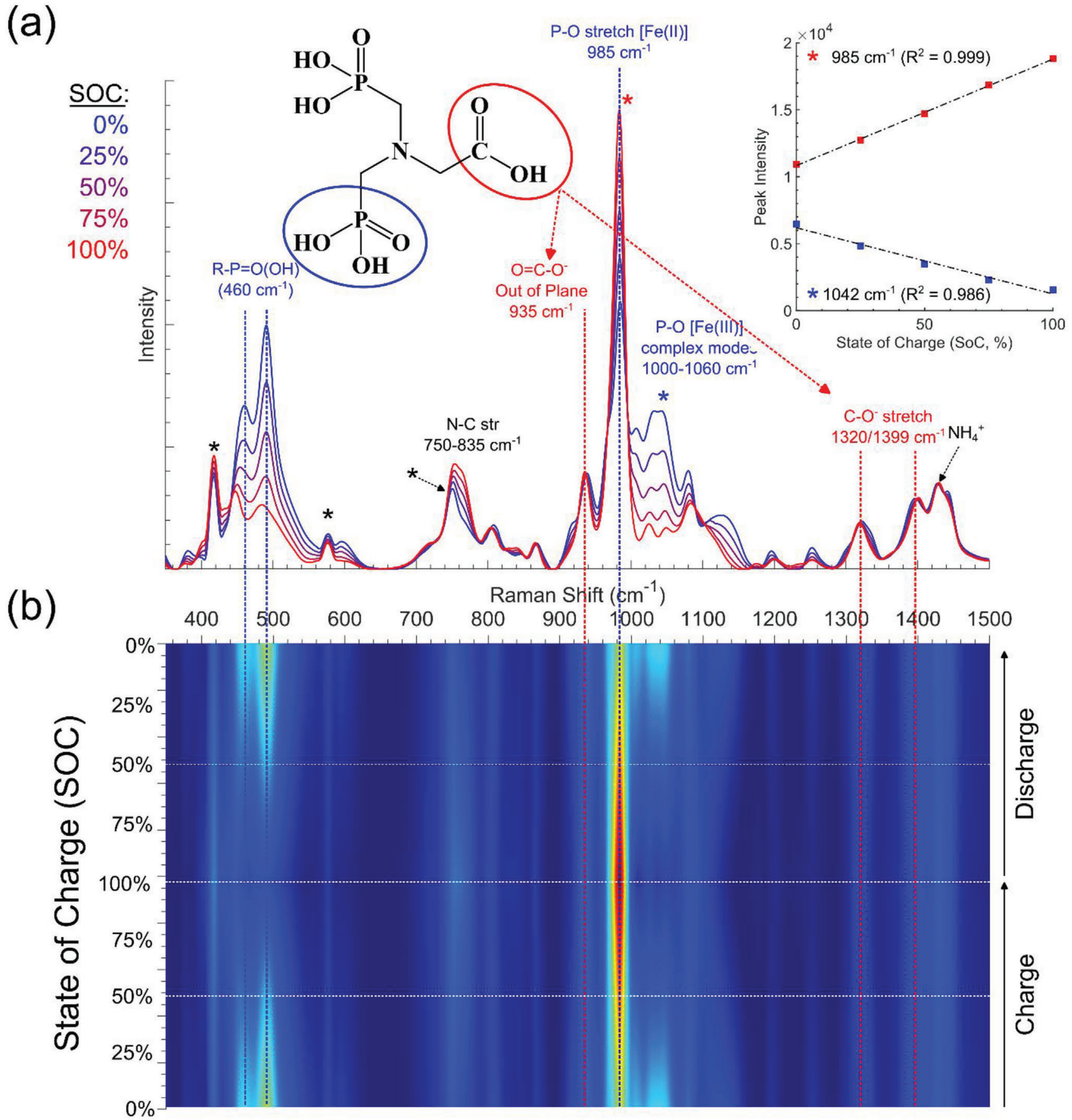

Figure 6. *Operando* Raman spectroscopy measurement. a) peak assignment and intensity evolution for selected Raman spectra at SOC (0, 25, 50, 75, and 100%). Characteristic Raman peaks belonging to carboxylate group are marked in red dotted line. Red and blue asterisks are Raman bands from P—O bonds of Fe(II) and Fe(III) complexes, respectively. The bands marked with black asterisk are the characteristic Raman bands from the sapphire lens used in the *operando* Raman flow-through cell setup. b) Intensity map for Raman spectrum for a complete cycle (charge and discharge). SOC 0–100% corresponds to the charge process, and 100–0% to the discharge process.

effective raw materials, i.e., glycine, formaldehyde, and phosphorous acid via Mannich-Type reaction.[22] It is worth noting that glycine has long been synthesized via the Strecker synthesis method, utilizing formaldehyde, ammonia, and hydrogen cyanide, and has been an established industrial process for decades. Reacting formaldehyde and ammonia produces intermediates which in presence of hydrogen cyanide yields 2-aminoacetonitrile that on hydrolysis is converted to glycine.[23] The synthesis pathways and the raw materials utilized are summarized in supporting information Figure S11 (Supporting

Information), showing easy of scalability and industrial production. Hence, BPMG offers similar cost advantages and scalability in comparison to NTMPA, but with higher voltage output and faster redox kinetics, thus position itself as a promising anolyte for all soluble Fe-RFB applications.

3. Conclusion

In summary, a new Fe complex synthesized from $FeCl_3$ and BPMG shows promise as an anolyte for near pH-neutral aqueous Fe-RFB systems. Compared to the previously reported NTMPA-based anolyte, $Fe(BPMG)_2$ anolyte offers a higher voltage output by 0.07 V (10% increase), attributed to its more negatively shifted redox potential. Full cell testing consisting of 0.3 M $Fe(BPMG)_2$ anolyte and 0.3 M $Fe(CN)_6$ catholyte showed an outstanding cycling stability (<0.0001%/cycle) with 100% CE over a long-term testing of 730 consecutive cycles (25 days) at a current density of 20 mA cm^{-2} (CC+CV mode). If one just considers the possible capacity degradation from the CC portion of the long-term cycling, the charge capacity degradation is <0.0001%, which is much smaller than 0.008%/cycle calculated for the discharge. A symmetric current testing reveals a general decrease in charge and discharge capacity while increasing the current density from 5 to 240 mA cm^{-2} due to the mass transfer limit. Upon decreasing the current to lower values, this $Fe(BPMG)_2$ electrolytes exhibit a good capacity recovery, indicating its excellent stability and resistance to decomposition under high current charge and discharge.

Based on DFT results, the most probable ligand coordination structure of $Fe(BPMG)_2$ complexes in the S1 state involves the bonding of two phosphonate groups from each BPMG ligand in a bidentate + monodentate configuration with the Fe ion, while leaving the carboxylate group unbound. *Operando* Raman measurements show Raman bands associated with the carboxylate group, such as those at 935 cm^{-1} ($-COO^-$ out-of-plane mode) and 1320/1399 cm^{-1} ($C-O^-$ stretch mode), exhibit no changes in intensity or peak position. In contrast, the P–O stretch at 985 cm^{-1} linked with $Fe(II)(BPMG)_2$ complexes shows a trend of intensification with increasing SOCs. Conversely, the P–O band associated with its oxidized form, $Fe(III)(BPMG)_2$, typically observed between 1000–1060 cm^{-1}, displays an opposite trend, with its intensity decreasing as SOC increases. Therefore, DFT and Raman results support $Fe(BPMG)_2$ complexes exhibit a similar molecular structure (S1) for both Fe(II) and Fe(III) states, in contrast to its all-phosphonate form, NTMPA. Consequently, the need for ligand reorientation is minimized in $Fe(BPMG)_2$ complexes, which is crucial for alleviating the slow redox reaction kinetics observed in $Fe(NTMPA)_2$ anolyte, where significant ligand reorientation occurs between Fe(II) and Fe(III) complexes. From materials perspective, $Fe(BPMG)_2$ electrolytes can be synthesized from resource abundant and cost effective materials, such as ammonia, formaldehyde, and ferric trichloride, with well-established synthesis routes, which can be easily demonstrated at a large scale. The exploration of redox potential shifts, electron transfer kinetics, and ligand reorientation within BPMG compared to NTMPA not only reveals improved flow battery cycling metrics but also offers a pathway to deepen our fundamental comprehension of coordination complexes in redox chemistry.

4. Experimental Section

Chemicals and Materials: Iron Fe(III) trichloride hexahydrate (Aldrich), ammonium chloride (Alfa Aesar), ammonium hydroxide (Thermo scientific), potassium hydroxide (Sigma-Aldrich), potassium chloride (Sigma-Aldrich), N,N-Bis(phosphonomethyl)glycine (BMPG, Aldrich), sodium ferrocyanide decahydrate (Acros Organics), and potassium ferrocyanide trihydrate (Acros Organics) were used as received.

Preparation of $Fe(BPMG)_2$ Complex: To prepare 10 mL of 0.3 M Fe(III)-$BPMG_2$ ($Fe(BPMG)_2$) complex with Fe/BPMG ratio of 1/2, 0.811 g of Fe(III) trichloride hexahydrate was initially dissolved in 3 mL deionized (DI) water in a beaker and kept under stirring. Simultaneously, 1.578 g of BPMG was also dissolved in 3 mL DI water in a different beaker, and 0.8 mL of 1.2 M ammonium hydroxide solution added to it, which was stirred for 30 min. Subsequently, the BMPG solution was slowly added using a pipette to the beaker containing Fe(III) trichloride solution. More water and 1.6 mL ammonium hydroxide (2.4 M) solution were added to dissolve the precipitate formed. Excess water was evaporated to achieve the targeted volume and concentration. A small amount of ammonium hydroxide was also added as needed to achieve the preferred near-neutral pH. For higher concentration $Fe(BPMG)_2$ electrolyte synthesis, ammonium hydroxide was substituted with potassium (K^+) hydroxide solution when preparing complex with K^+ cation.

Preparation of Fe Catholytes: Seven milliliters of 0.3 M ferrocyanide, $Fe(CN)_6$, catholyte was prepared by dissolving 0.508 g of sodium ferrocyanide decahydrate and 0.444 g of potassium ferrocyanide trihydrate in 7 mL of DI water with 0.524 g ammonium chloride added as a supporting electrolyte aiming to achieve NH_4^+ concentration (1.4 M) balance between the anolyte and catholyte.

Cyclic Voltammetry Measurement: Cyclic voltammetry (CV) measurements were employed to investigate the electrochemical properties of the $Fe(BPMG)_2$ complex. A three-electrode cell setup using activated glassy carbon (dia. 3 mm) as the working electrode, glassy carbon rod as the counter electrode, and Ag/AgCl reference electrode, was utilized for CV measurements. The CVs were run over various potential ranges at different scan rates and the data recorded by electrochemical workstation (CHI660E potentiostat).

Glassy Carbon (GC) Electrode Activation: The GC electrode was polished using alumina slurry, sonicated and cleaned with DI water before activation. Subsequently, the electrochemical activation of the electrode surface was carried out in 2 M sulfuric acid (H_2SO_4) and potential scanning performed in the potential range 0 to 2.0 V at scan rate of 100 mV s^{-1} for 10 consecutive cycles. A standard three-electrode setup was also employed in this process.

Flow Battery Cell Assembly and Test: The flow cell was assembled using electrolyte reservoirs, cell stack and a pump. The flow frame in the cell stack utilizes an interdigitated flow field design with active area of 10 cm^2. A Nafion membrane (NR212) was employed to separate the two half-cells. Prior to use, the NR212 membrane was soaked in ammonium hydroxide or potassium hydroxide solution overnight to convert to NH_4^+ /K^+ form. Two carbon papers (2 cm × 5 cm, FreudenbergH23) and 2 ELAT (2 cm × 5 cm, Nuvant) were used as negative electrode. Similarly, 3 ELAT (2 cm × 5 cm, Nuvant) were used as the positive electrode. The electrolyte containers and the cell stack were connected using Masterflex tubes via. a Masterflex L/S peristaltic pump (Cole-Parmer), which was used to circulate the electrolytes through cell stack with different flow rates. The flow battery was set up with 7 mL of 0.3 M $Fe(BPMG)_2$ as the anolyte and 7 mL of 0.3 M $Fe(CN)_6$ in 1.4 M NH_4Cl as the catholyte that were circulated at a flow rate of 40 mL min^{-1}. Based on one-electron redox reaction, the theoretical capacity of 7 mL 0.3 M $Fe(BPMG)_2$ anolyte was ≈56 mAh. The battery testing was conducted with discharge and charge cut-off voltages set at 0.3 and 1.0 V, respectively. The charging process comprises a constant current (CC) charge, e.g., 200 mA (20 mA cm^{-2}), during which the battery was charged to the charge cut-off voltage (1.0 V), followed by a constant voltage (CV) charge that holds the voltage at 1.0 V until the current reaches 10 mA. The discharge was done in a similar way, consisting of CC and CV discharge until the discharge current reaches 10 mA. Symmetric and asymmetric battery testing were conducted at various current density ranging from 5 to 240 mA cm^{-2}. Cell testing was conducted within a N_2-purged box at room temperature using an Arbin BT-200 battery cycler.

Pulse-Rest Measurement: Pulse-rest experiments were performed for a flow battery consisting of 0.3 M $Fe(BPMG)_2$ anolyte and $Fe(CN)_6$ catholyte. During each current-on (pulsed charge or discharge) period, a current of 20 mA cm^{-2} was applied for 33 s. The subsequent current-off (relaxation) period was 180 s, which was sufficient for the voltage to be relaxed to the equilibrium. The open circuit voltage (OCV) profiles of the charge and discharge processes were obtained by choosing the voltage value at the end of each relaxation period.

X-Ray Absorption Spectroscopy (XAS): Fe K-edge X-ray absorption near-edge spectroscopy (XANES) data were acquired to assess the oxidation state in liquid $Fe(BPMG)_2$. The experimentation utilized a benchtop easyXAFS300 instrument (easyXAFS). For specified states of charges (SOCs), minute quantities of $Fe(BPMG)_2$ anolytes were extracted and introduced into a liquid cell designed to handle air-sensitive electrolytes. Subsequently, the liquid cell, housing $Fe(BPMG)_2$ anolytes at various SOCs, was inserted into the easyXAFS300 instrument for XAF measurements. Fe K-edge spectra were captured using a Ge(620) spherically-bent crystal analyzer and a Mo anode X-ray tube operating at 25 kV voltage and 20 mA current. Consistent power settings were employed for all spectra, encompassing both sample and background scans. Throughout the experiments, the silicon drift detector deadtime was diligently maintained below 30%.

Electrochemical Impedance spectroscopy (EIS): EIS measurements were performed with a Gamry Reference 600+ potentiostat using a frequency range generally from 100 kHz to 0.1 Hz. An AC voltage amplitude of 10 mV was employed. Before each measurement, the cell was rested for ≈10 min at the end of charge or the end of discharge in order to reach equilibrium. Z-view software is used to fit the impedance spectra using a circuit consisting of R_1 (Ohmic resistance), R_2 (Charge transfer resistance), a CPE (constant phase element), and a Warburg.

Operando Raman Spectroscopy: Operando Raman Spectroscopy experiments were performed using a Mettler-Toledo (Columbus, OH) ReactRaman785 All-in-One spectrometer with a 785 nm solid-state laser for excitation. The anolyte side of the cell was connected to a Marqmetrix (Seattle, WA) BallProbe Flow Cell as the Raman sampling interface to probe the flow path of the anolyte during charging and discharging. Raman spectra were acquired at regular sampling intervals (10 averages, 2 or 3 s per spectrum depending on analyte concentration and signal intensity). Raw spectra were processed using a smoothing function (Savitzky-Golay filter) followed by baseline subtraction using a polynomial fit of the baseline. Then, spectra could be aligned temporally with a given charge/discharge cycle for analysis of chemical trends as a function of the state of charge of the cell.

Density Function Theory (DFT): Density functional theory (DFT) was calculated using ORCA version 4.2.1,[24] and the minimally augmented triple-ζ basis set with one set of polarization functions (ma-def2-TZVP) was used for this work. The aqueous solvent environment was accounted for using the universal solvation model (SMD) for water. Geometry optimization was carried out in implicit aqueous environment using the B3LYP exchange correlation functional with Grimme's D3 dispersion correction with Becke-Johnson damping.

Supporting Information

Supporting Information is available from the Wiley Online Library or from the author.

Acknowledgements

This work was funded by the U.S. Department of Energy (DOE) Office of Electricity (OE) under contract DE-AC06-76LO1830 through Pacific Northwest National Laboratory (project #70247). Pacific Northwest National Laboratory is operated by Battelle for the DOE under Contract DE-AC05-76RL01830. G.L. and D.B. also extend their thanks to John L. Fulton and Timothy C. Droubay for their assistance in preparing the instrument for D.B. to collect XAS data.

Conflict of Interest

A non-provision patent related to this work titled "Iron complexes with phosphonate-based ligands as RFB anolyte materials" has been filed by PNNL. P.S.R., J.M.W., D.B. declare no competing interests.

Data Availability Statement

The data that support the findings of this study are available in the supplementary material of this article.

Keywords

aqueous flow battery, iron complex, iron flow battery, neutral pH, phosphonate ligand

Received: July 18, 2024
Revised: September 28, 2024
Published online: October 20, 2024

[1] G. L. Soloveichik, *Chem. Rev.* **2015**, *115*, 11533.
[2] J. Winsberg, T. Hagemann, T. Janoschka, M. D. Hager, U. S. Schubert, *Angew. Chem., Int. Ed.* **2017**, *56*, 686.
[3] B. Dunn, H. Kamath, J.-M. Tarascon, *Science* **2011**, *334*, 928.
[4] a) M. Ulaganathan, V. Aravindan, Q. Yan, S. Madhavi, M. Skyllas-Kazacos, T. M. Lim, *Adv. Mater. Interfaces* **2016**, *3*, 1500309; b) M. Skyllas-Kazacos, M. Chakrabarti, S. Hajimolana, F. Mjalli, M. Saleem, *J. Electrochem. Soc.* **2011**, *158*, R55; c) K.-L. Huang, X.-G. Li, S.-Q. Liu, N. Tan, L.-Q. Chen, *Renewable Energy* **2008**, *33*, 186.
[5] M. Vijayakumar, W. Wang, Z. Nie, V. Sprenkle, J. Hu, *J. Power Sources* **2013**, *241*, 173.
[6] a) H. Zhang, C. Sun, *J. Power Sources* **2021**, *493*, 229445; b) S. Yu, X. Yue, J. Holoubek, X. Xing, E. Pan, T. Pascal, P. Liu, *J. Power Sources* **2021**, *513*, 230457.
[7] M. C. Tucker, A. Phillips, A. Z. Weber, *ChemSusChem* **2015**, *8*, 3996.
[8] a) D.-Y. Wang, R. Liu, W. Guo, G. Li, Y. Fu, *Coord. Chem. Rev.* **2021**, *429*, 213 650; b) K. L. Hawthorne, J. S. Wainright, R. F. Savinell, *J. Electrochem. Soc.* **2014**, *161*, A1662.
[9] a) A. Lê, D. Floner, T. Roisnel, O. Cador, L. Chancelier, F. Geneste, *Electrochim. Acta* **2019**, *301*, 472; b) K. Gong, F. Xu, J. B. Grunewald, X. Ma, Y. Zhao, S. Gu, Y. Yan, *ACS Energy Lett.* **2016**, *1*, 89.
[10] a) P. S. Borchers, M. Strumpf, C. Friebe, I. Nischang, M. D. Hager, J. Elbert, U. S. Schubert, *Adv. Energy Mater.* **2020**, *10*, 2 001 825; b) Y. Ding, Y. Zhao, Y. Li, J. B. Goodenough, G. Yu, *Energy Environ. Sci.* **2017**, *10*, 491; c) J. Luo, M. W. Hu, W. D. Wu, B. Yuan, T. L. Liu, *Energy Environ. Sci.* **2022**, *15*, 1315.
[11] J. Luo, B. Hu, C. Debruler, Y. Bi, Y. Zhao, B. Yuan, M. Hu, W. Wu, T. L. Liu, *Joule* **2019**, *3*, 149.
[12] a) D. Xi, A. M. Alfaraidi, J. Gao, T. Cochard, L. C. Faria, Z. Yang, T. Y. George, T. Wang, R. G. Gordon, R. Y. Liu, *Nat. Energy* **2024**, *9*, 479; b) X. Li, P. Gao, Y.-Y. Lai, J. D. Bazak, A. Hollas, H.-Y. Lin, V. Murugesan, S. Zhang, C.-F. Cheng, W.-Y. Tung, *Nat. Energy* **2021**, *6*, 873; c) W. Q. Ruan, J. T. Mao, S. D. Yang, Q. Chen, *J. Electrochem. Soc.* **2020**, *167*, 100543.
[13] S. E. Waters, B. H. Robb, M. P. Marshak, *ACS Energy Lett.* **2020**, *5*, 1758.

[14] P. Schröder, N. Aguiló-Aguayo, D. Obendorf, T. Bechtold, *Electrochimica Acta* **2022**, *430*, 141042.
[15] P. Tippayamalee, C. Pattanathummasid, R. Chanajaree, P. Pienpinijtham, S. Kheawhom, R. Cheacharoen, *J. Energy Storage* **2024**, *86*, 111295.
[16] G. S. Nambafu, A. M. Hollas, S. Zhang, P. S. Rice, D. Boglaienko, J. L. Fulton, M. Li, Q. Huang, Y. Zhu, D. M. Reed, *Nat. Commun.* **2024**, *15*, 2566.
[17] a) X. Q. Liu, T. Y. Li, Z. Z. Yuan, X. F. Li, *J. Energy Chem.* **2022**, *73*, 445; b) K. Gong, F. Xu, J. B. Grunewald, X. Y. Ma, Y. Zhao, S. Gu, Y. S. Yan, *ACS Energy Lett.* **2016**, *1*, 89.
[18] J. Noack, N. Roznyatovskaya, J. Kunzendorf, M. Skyllas-Kazacos, C. Menictas, J. Tübke, *J. Energy Chem.* **2018**, *27*, 1341.
[19] D. K. Gosser, *Cyclic Voltammetry: Simulation and Analysis of Reaction Mechanisms*, Vol. *43*, Wiley VCH, New York **1993**.
[20] I. Bertini, C. Luchinat, G. Parigi, *Solution NMR of Paramagnetic Molecules: Applications to Metallobiomolecules and Models*, Elsevier, Amsterdam **2001**.
[21] G. Socrates, *Infrared and Raman Characteristic Group Frequencies: Tables and Charts*, John Wiley & Sons, Hoboken, NJ **2004**.
[22] a) F. Xu, L. Zhong, Y. Xu, C. Zhang, P. Wang, F. Zhang, G. Zhang, *Cellulose* **2019**, *26*, 7537; b) K. Moedritzer, R. R. Irani, *J. Org. Chem.* **1966**, *31*, 1603.
[23] S. W. Fox, C. R. Windsor, *Science* **1970**, *170*, 984.
[24] F. Neese, F. Wennmohs, U. Becker, C. Riplinger, *J. Chem. Phys.* **2020**, *152*, 224108.